High aspect ratio x-ray waveguide channels fabricated by e-beam lithography and wafer bonding

H. Neubauer, S. Hoffmann, M. Kanbach, J. Haber, S. Kalbfleisch, S. P. Krüger, and T. Salditt

Citation: Journal of Applied Physics **115**, 214305 (2014); doi: 10.1063/1.4881495
View online: http://dx.doi.org/10.1063/1.4881495
View Table of Contents: http://scitation.aip.org/content/aip/journal/jap/115/21?ver=pdfcov
Published by the AIP Publishing

High aspect ratio x-ray waveguide channels fabricated by e-beam lithography and wafer bonding

H. Neubauer, S. Hoffmann, M. Kanbach, J. Haber, S. Kalbfleisch, S. P. Krüger, and T. Salditt[a)]
Institut für Röntgenphysik, Universität Göttingen, Friedrich-Hund-Platz 1, 37077 Göttingen, Germany

(Received 14 April 2014; accepted 17 May 2014; published online 3 June 2014)

We report on the fabrication and characterization of hard x-ray waveguide channels manufactured by e-beam lithography, reactive ion etching and wafer bonding. The guiding layer consists of air or vacuum and the cladding material of silicon, which is favorable in view of minimizing absorption losses. The specifications for waveguide channels which have to be met in the hard x-ray range to achieve a suitable beam confinement in two orthogonal directions are extremely demanding. First, high aspect ratios up to 10^6 have to be achieved between lateral structure size and length of the guides. Second, the channels have to be deeply embedded in material to warrant the guiding of the desired modes while absorbing all other (radiative) modes in the cladding material. We give a detailed report on device fabrication with the respective protocols and parameter optimization, the inspection and the optical characterization. [http://dx.doi.org/10.1063/1.4881495]

I. INTRODUCTION

Hard x-ray nanobeams with cross sections in the range of $d \simeq 10$–100 nm enable novel nanoscale analytic techniques, adding nanoscale real space resolution to x-ray spectroscopy and diffraction, and enabling novel variants of coherent imaging and holography. A variety of optical elements can be used to generate x-ray nanobeams, such as Fresnel zone plates,[1–4] multilayer Laue lenses,[5] multilayer zone plates,[6] compound refractive lenses,[7–9] curved mirrors (e.g., in Kirkpatrick-Baez (KB) geometry[10,11]), or x-ray waveguides,[12–17] as well as combinations of these elements.[6,18,19] The different optical elements impose significant challenges for nanostructuring and metrology, and progress in this field is often limited by the corresponding bottlenecks in fabrication. This is particularly the case for x-ray waveguides (WG), which deliver coherence filtered x-ray radiation with nanoscale dimensions in one spatial (1DWG)[12–17,20,21] or two spatial dimensions (2DWG).[22–24]

Depending on the materials employed for the guiding and cladding layers, waveguides are capable to deliver beams of about 10 nm in cross section,[25] comparable to the record values achieved by other types of focusing optics.[6,26] By tailoring the coherence properties and cross section of x-ray beams, waveguides can extend the function of macroscopic slits and pinholes of conventional x-ray experiments to x-ray nanobeam optics. In particular, in the monomodal regime they also enable the control of the wavefront phase highly desirable for coherent x-ray imaging and holography.[24,27–29] To block the multi-keV photon energy beam in the cladding material, rather long channels are needed with aspect ratios in the range of 10^4–10^6, depending on the photon energy E and cross section d.

X-ray propagation in waveguide channels has been studied both analytically[30–32] and by finite difference (FD) simulations,[17,32–34] including generalizations to more complex structures and effects including both thickness variations and roughness,[35,36] which illustrate the challenges associated with fabrication.

In particular, the extreme aspect ratios required for x-ray waveguides impose tremendous challenges in fabrication. Note that one-dimensional beam confinement can be easily achieved by planar waveguides (1DWG) fabricated by thin film deposition,[37] but is only of limited use. The vast majority of applications, in particular holographic imaging, requires two-dimensional waveguides (2DWG), as first demonstrated by Pfeiffer *et al.*,[22] however, with impractically low efficiencies, or at the expense of an inherent astigmatism in the case of planar waveguides in crossed geometry.[37] When replacing the coupling geometry and combining the waveguides with high gain pre-focusing KB mirrors, the waveguide exit flux was increased to $I_{wg} \simeq O(10^6)$ photons per second,[23,24] which is still too low for most imaging applications, e.g., holography experiments. In earlier approaches, the waveguide channels consisted of polymer stripes defined by e-beam lithography and coated with a silicon cladding.[23,24] Ideally, however, waveguide channels should be empty (air, vacuum), since a solid core material leads to unnecessary absorption, unwanted phase front modulations based on density variations, and in the case of polymer channels also drifts resulting from beam damage in the core material. To overcome these problems, a novel fabrication scheme based on dry etching of channels into silicon wafers has been reported previously,[38,39] using an etch mask defined by e-beam lithography, removal of the mask and subsequent capping by a second wafer bonded on top of the first. However, only μm-sized cross sections were achieved in both directions. Only recently, this fabrication approach was optimized and refined to achieve control over both interface

[a)]Electronic mail: tsaldit@gwdg.de

quality and channel dimensions in the relevant sub-100 nm range. In fact, first x-ray imaging results obtained with such a channel have been presented,[18] without giving the details and refinements of the fabrication process, which is the scope of the present paper. Here, we give the first report on the fabrication of wafer-bonded 2DWG channels in the relevant sub-100 nm range, addressing the detailed steps and protocols as well as including the most recent optimizations which result in a waveguide exit flux of $I_{wg} \simeq O(10^8)$ ph/s, as measured at the P10 beamline of the PETRA III storage ring of DESY for a recently fabricated waveguide channel presented here.

II. EXPERIMENTAL METHODS: FABRICATION

Fig. 1(a) shows a schematic representation of the waveguide fabrication steps. An electron beam resist spin-coated on a silicon wafer is structured by electron beam lithography, providing an etching mask. The structure is transferred into the substrate by reactive ion etching (RIE). Subsequently, the mask is removed and a second wafer is attached by hydrophilic wafer bonding[40] under cleanroom conditions. As a substrate, one-sided polished $1000 \pm 25\,\mu$m thick 4 in. (100) Si-Wafers (silchem) have been used. The fabrication steps have been carried out at varied parameters, as presented in Table I. In the following, we describe the process based on the parameters of protocol I, given as an example. We will refer to the parameters of the other protocols where appropriate. The poly-methyl-methacrylate (PMMA) e-beam resist "A2" (MicroChem) was spincoated onto the substrate at 2000 revolutions per minute (rpm), providing a 100 nm layer of positive e-beam resist. The resist was exposed with the lithographic pattern of parallel channels, as depicted in Fig. 4(b). The exposure was performed by a Raith e_LiNE lithography system using the Fixed Beam Moving Stage (FBMS) exposure mode, moving an interferometric laser stage below a stationary electron beam, thus avoiding the necessity of write-field stitching. Note that only this approach enables for the production of high aspect ratio waveguide channels in the first place, as the mismatch from write-field stitching typically exceeds the waveguide channel dimension. The structures were developed in a 1:3 mixture of methylisobutylketone (MIBK): isopropanol (IPA), with a typical volume of 80 ml, to which 1.6 ml of distilled water was added. The samples were kept in the developer for 30 s at a temperature of 10 °C, followed by 30 s in IPA at room temperature, serving as a stopper.[41] Subsequently, the sample was rinsed in a nitrogen gas flow. The structure was transferred into the substrate by reactive ion etching (Plasmalab System 100, Oxford Instruments Plasma Technologies), applying a 40 sccm CHF_3 and 10 sccm SF_6 gas flow at a power of 100 W for 48 s at room temperature, or a variation of this recipe. Alternatively, a mixture of SF_6 and CF_4 can be used, yielding results of comparable quality both in etching depth and profile. Part of the wafer area was covered by an additional aluminum foil mask in order to increase the etching rate and to assure uniformity, yielding etching depths of 30–80 nm, depending on the protocol. The subsequent mask removal involved a 20 min acetone bath at 50 °C, a distilled water, IPA and dry nitrogen rinse, followed by a 20 min IPA bath at 50 °C and a final nitrogen rinse. In

TABLE I. Fabrication parameters, according to the different protocols (I–IV) evolving from iterations in fabrication and characterization: spincoating velocity, etching gas composition and etching time, cleaning procedure before bonding, annealing temperature, and time. All other parameters were kept constant. In addition, the channel depth evaluated after dicing from SEM micrographs is shown.

	Coating (rpm)	SF_6:CHF_3 (sccm)	Cleaning	Bonding	Channel depth (nm)
I	2000	14:35 (30 s)	O_2 (30 min)	1050 °C (4 h)	24
II	2000	10:40 (40 s)	RCA-SC1	1050 °C (4 h)	30
III	2000	14:35 (40 s)	RCA-SC1	1050 °C (4 h)	50
IV	1000	14:35 (50 s)	RCA-SC1	750 °C (2 h)	70

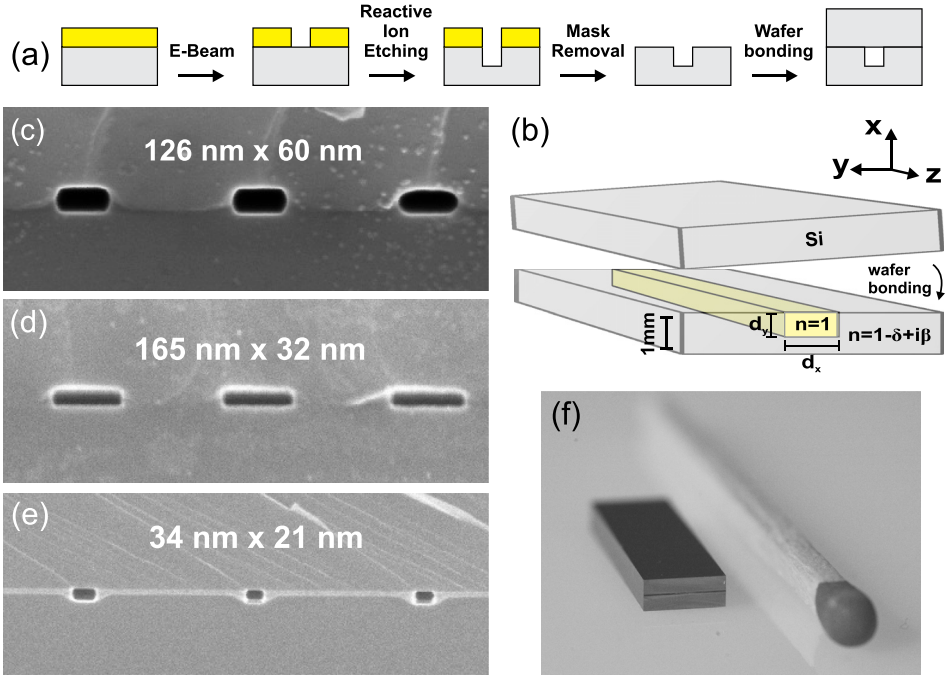

FIG. 1. (a) Sketch of waveguide processing sequence: resist deposition, e-beam exposure, reactive ion etching, mask removal, and finally wafer bonding. (b) Schematic of air-filled channel capped by a top wafer bonded to the substrate. ((c)–(e)) SEM micrographs of waveguide channel entrances, with (d) comparable to the waveguide used for Fig. 5. (f) Photograph of waveguide chip as cut by the wafer dicing machine.

order to ensure a clean wafer surface, this step was followed in protocol I by a 30 min RIE plasma cleaning, using 50 sccm O_2 at a power of 300 W at room temperature, which also served as a hydrophilization of the wafer surface in order to enhance bonding strength.

Since the O_2 plasma treatment was found to affect the channel shape function and interface quality during the high temperature annealing step of wafer bonding, plasma cleaning time was therefore reduced or omitted in other protocols. Note that plasma exposure can introduce defects and dislocations to the silicon oxide layer after a few seconds.[42] Instead, a dip in a DI water bath for a few minutes and a 15 min RCA-SC1 clean[43] at 65 °C can be used to ensure surface cleanliness. Furthermore, to avoid the formation of voids between the two bonded wafers originating from the thermal decomposition of surface contaminants or the desorption of hydrogen,[42] a reduced annealing temperature[44] was chosen in protocol IV.

In order to convert the etched surface pattern into buried channel structures, a second, clean Si wafer of the same batch was attached to the structured wafer manually, promoting a van-der-Waals type pre-bonding, followed by formation of covalent bonds in a thermal furnace (L9/13/P320, Nabertherm) under air atmosphere.[40] The sample was heated at a rate of 3 °C/min from room temperature up to 1050 °C. Temperature was kept constant at 1050 °C for 4 h, and the sample was cooled down to room temperature inside the furnace over a period of 10 h. During the thermal treatment, the sample was positioned on three ceramic distance pieces, ensuring optimum heat flow. In a wafer dicing machine (DAD 321, DISCO), the samples were finally cut to a width of 5 mm and a length l, depending on the requirements of the experiment, in particular, the photon energy. For the results reported here, lengths of $l = 1.0$ mm (7.9 keV), $l = 5.24$ mm (13.8 keV) and $l = 13$ mm (17.5 keV), were chosen for the respective experiments. The blade (NBC-ZB 1070, 150 μm thickness, 5 μm grain size, DISCO) was operated at a feed rate of 0.5 mm/s and a positioning precision of 10 μm. As a direct cut through the sample results in material smearing and also often clogging of the channel openings resulting from blade roughness, the sample was cut from both sides, leaving a section of 100 μm thickness connecting the two pieces. By applying a slight pressure, the connection can be broken, yielding sufficiently clean and open waveguide entrances. Optionally, a focused ion beam (FIB) source (Nova Nano Lab 600, FEI) was used to further clean the 17.5 keV samples on both waveguide entrance and exit by successive silicon ablation. Thus, any deviation from the ideal waveguide shape, which may have occurred due to deformations during the breaking, can be corrected.

Structures have been investigated in view of changes in structure width and roughness during the fabrication process. Fig. 2 shows SEM micrographs for the processing steps of exposure and development, etching and mask removal, as well as thermal treatment for one and the same structure. Note that this last step was performed without a capping wafer for inspection purposes, as enclosed channels will not be easily accessible by SEM anymore. Interestingly, during the annealing process a strong decrease in both channel width and roughness is observed. The smaller the original structure, the more pronounced this effect becomes. We attribute this effect to a diffusion-driven rearrangement of surface atoms, fed by the energy provided by thermal treatment. As the system tends to minimize its free surface energy, channel wall roughness will be reduced, hence structures improve in quality. Consequently, the reduction in channel width has to be taken into account when choosing an appropriate pattern for exposure, as narrow channels might close while thermally treated. If, in spite of this effect, a further reduction of line width is required, the temperature of the developer can be reduced.[41] Thus, the development of partially exposed areas at the edge of the structure is prevented, and the resulting pattern will be as precise as defined by means of electron lithography.

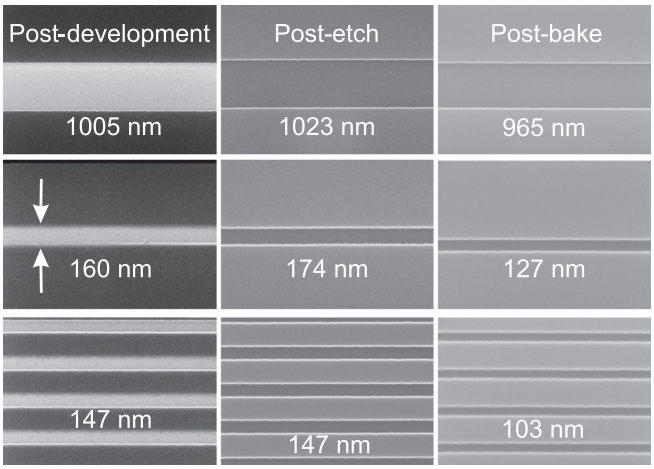

FIG. 2. Evolution of structure width and roughness during fabrication, for different initial channel widths. SEM micrographs, from left to right: Resist after development, etched structure after mask removal and structure after thermal treatment (without capping wafer). Both structure width and sidewall roughness are decreased significantly during heating.

Additionally, after performing the pre-bond processing step of attaching the two wafer surfaces to each other, an infrared camera was used for sample inspection, see Fig. 3(a). As even the enclosure of a 1 μm-sized dust particle may result in a mm-sized air bubble preventing a successful bonding,[40] samples were inspected using an InGaAs-near-infrared camera (XS-Base, Xenics) at different magnifications. If an air bubble is detected, it can be removed manually by applying an external pressure to the sample, see Figs. 3(b) and 3(c), or the pre-bonded sample can be reopened with the help of a razor blade in order to exchange the capping wafer. Figs. 3(d) and 3(e) shows embedded structures after the annealing step, localizing 500 nm sized features. Thus, the correct position of the embedded structures after dicing the sample can be verified easily.

III. EXPERIMENTAL CHARACTERIZATION

Waveguide optical characterization was performed at the undulator beamline ID22Ni of ESRF, Grenoble, and at the GINIX (Göttingen Instrument for Nano-Imaging with X-rays) instrument of beamline P10 of DESY, Hamburg.[45,46] Fig. 4(a) shows a schematic of the experimental setup, which in both cases used a KB mirror system to focus the beam

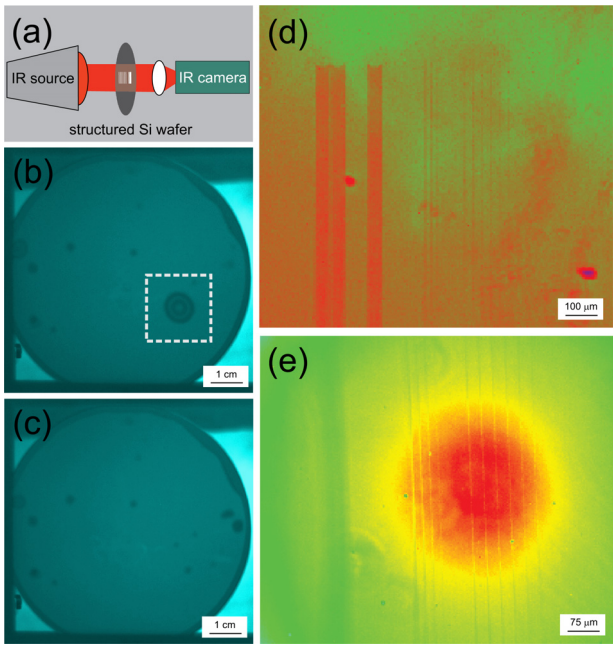

FIG. 3. (a) Inspection of structures embedded in bonded silicon wafers by infrared light in transmission geometry. (b) Wafer with enclosed air bubbles (highlighted by dashed line). (c) Wafer after defined removal of one specific air bubble. (d) Embedded structures in 20× magnification. (e) Embedded structures in 40× magnification (smallest visible structure 500 nm in width).

onto the waveguide entrance. At ID22Ni the focal spot size of the KB was $D_h = 129$ nm (FWHM) and $D_v = 166$ nm (FWHM), for the horizontal and vertical directions, respectively. The waveguide length $l = 13$ mm was optimized to the photon energy $E = 17.5$ keV, assuring sufficient absorption of the radiative modes.

At the GINIX endstation, two different settings were used for two beamtimes: (beamtime GINIX-1) $E = 7.9$ keV and $D_{h/v} = 530/520$ nm (FWHM), and (beamtime GINIX-2) $E = 13.8$ keV and focal spot size $D_{h/v} = 370/170$ nm (FWHM). For beamtime GINIX-1, the same waveguide as for the beamtime at ID22Ni was used, but diced to a shorter length $l = 1$ mm to account for the smaller energy. In order to simplify the waveguide alignment in the beam, the lithographic pattern was designed containing a number of parallel waveguide channels with a lateral periodicity of 30 μm, including a variation of the individual channel width (see Fig. 4(b)), as well as additional areas which act as one-dimensional planar waveguides (1DWG), since the corresponding channel width, i.e., 50 μm and 100 μm, respectively, was much larger than the beam, requiring only the fine alignment of one translation and one rotational degree of freedom.

Fig. 5 shows the measured farfield intensity distribution with corresponding simulations (GINIX-1 and ID22Ni). The settings and parameters for the presented farfield pattern were the following: (a) photon energy 7.9 keV, channel length 1 mm, pre-focusing with KB mirrors, direct illumination CCD detector (LCX, Princeton), exposure time 100 s (GINIX-1 setting), (d) photon energy 17.5 keV, channel length 13 mm, pre-focusing with KB mirrors, pixel detector (Maxipix, ESRF), exposure time 2 s (ID22Ni setting).

In (b) the modulus of the autocorrelation function obtained by inverse Fourier transform of the data shown in (a) is plotted. Gaussian fits to the peak center along the two principle axes yield a width (FWHM) of 69 nm (horizontal)

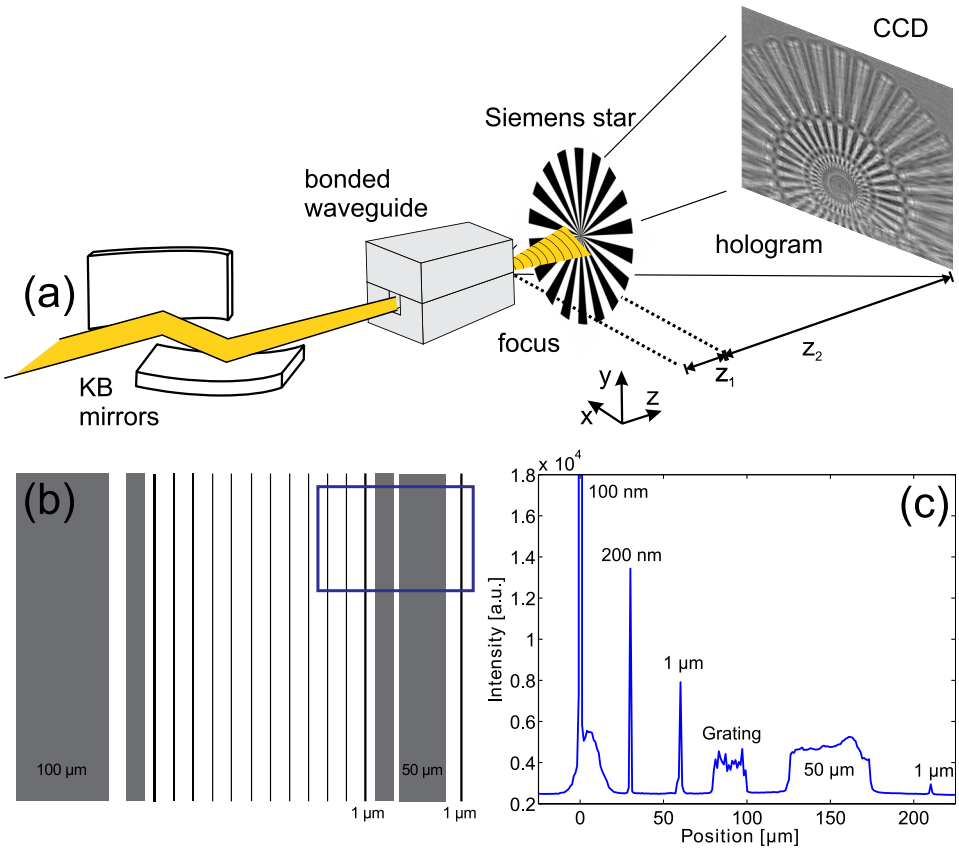

FIG. 4. (a) Holographic imaging setup as used in ESRF (ID22Ni) and PETRA III (GINIX, P10) experiments to determine the waveguide imaging resolution using a test structure.[18] (b) Typical layout, with several channels on the chip enabling higher throughput in the characterization of optical properties. In addition to the channels, larger structures are placed at the sides, facilitating the alignment of rotational and translational degrees of freedom. (c) Lateral (horizontal) scan helping to identify the individual channel positions as marked in (b), with rotations and vertical position optimized to the 100 nm channel.

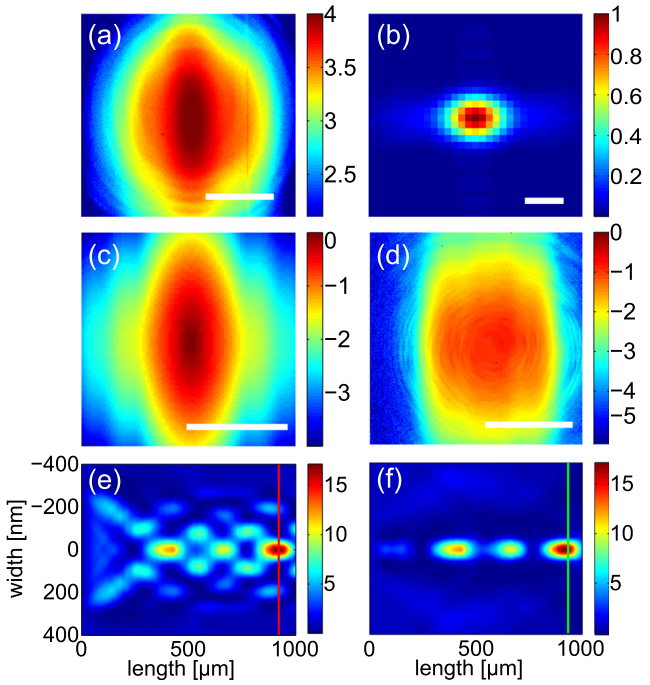

FIG. 5. Comparison of ((a), (b), (d)) experimental results with ((c), (e), (f)) numerical simulations for a 140 nm × 24 nm waveguide channel. (a) Farfield intensity distribution with logarithmically coded photon counts of a 100 s exposure recorded at 7.9 keV photon energy and waveguide channel length $l = 1$ mm (`GINIX-1` experimental settings). Scale bar: 0.1 deg. (b) Modulus of the autocorrelation function corresponding to the data shown in (a). Scale bar: 50 nm. (d) Farfield intensity distribution with logarithmically normalized intensity, as recorded over 2 s at 17.5 keV photon energy and waveguide channel length $l = 13$ mm (`ID22Ni` experimental settings). Scale bar: 0.1 deg. ((c), (e), (f)) Simulation results (finite difference calculations[33]) for $E = 17.5$ keV and $l = 13$ mm, corresponding to the experimental settings of ID22Ni. (c) The simulated farfield pattern obtained by the squared modulus of the Fourier transform of the calculated exit wave (nearfield). ((e), (f)) The simulated nearfield intensity distribution in the (e) *xz* and (f) *yz* plane of the channel, corresponding to the 140 nm and 24 nm wide directions, shown for the entrance section ($0 \le z \le 1$ mm) of the waveguide channel.

and 44.5 nm (vertical). The finite difference simulation[33] of the nearfield and corresponding farfield distribution, as obtained by the modulus squared of the Fourier transform of the nearfield, are shown in (c), corresponding to the parameters of the experiment shown in (d). In (e,f), the intensity distribution inside the waveguide channel (d) in the entrance region (first mm) is shown, namely by centered cuts in (e) the horizontal *xz* and (f) the vertical *yz* planes. Note that the multimodal propagation of the guided wave results in a periodic pattern significantly smaller than the channel width. Gaussian fits along the principal axes (see red and green lines) yield 18.2 nm and 17.2 nm for *xz* and *yz*, respectively. Multimodal propagation leads to a beating effect, i.e., periodic field patterns due to the superposition of the excited modes. In the horizontal direction with 140 nm channel width the number of modes is higher than in the vertical direction where the beam is confined by a channel height of 24 nm (see also Fig. 6). After about 900 μm, positive interference is particularly high for both planes simultaneously, yielding a plane of minimum beam width, as indicated by the red and green lines. This shows that beam confinement can be much smaller than the channel cross section in certain planes.

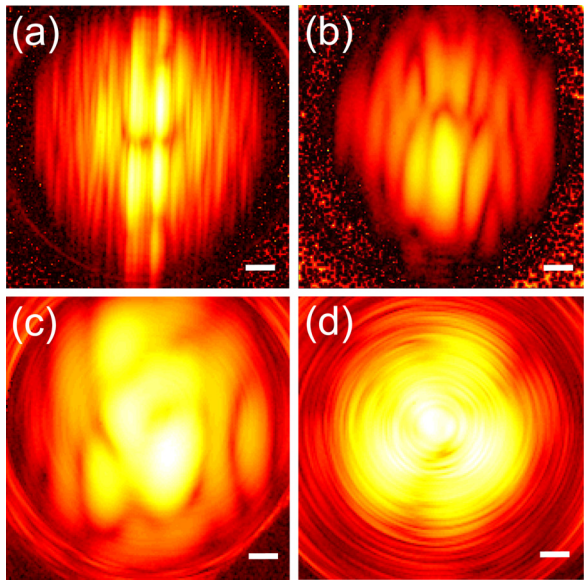

FIG. 6. Farfield intensities depending on waveguide width, using a waveguide chip of a length $l = 5.24$ mm. The beamline was operated at 13.8 keV. The intensity (logarithmic plot) was recorded within 1 s and is normalized to the maximum value of the intensity distribution shown in (d). Detector: Pilatus 300 K, ROI: 170 px × 170 px. Channel dimensions: (a) 982 nm × 82 nm, (b) 317 nm × 79 nm, (c) 153 nm × 73 nm, and (d) 82 nm × 67 nm, scalebars: 3 mm.

The broadening by diffraction reflects the nanometer scale beam collimation in the waveguide exit plane. The diffraction broadening is directly evident when comparing the two measured photon energies, 7.9 keV and 17.5 keV, respectively. Note that the same channel was measured in two consecutive experiments, the first at beamline `ID22Ni` of ESRF at 17.5 keV, the second at 7.9 keV at the nanofocus instrument `GINIX` at beamline P10/PETRA III at DESY. According to the requirements of photon energy in view of absorbing the radiation modes, the waveguide chip was cut to a length of $l = 13$ mm and $l = 1$ mm, respectively. The comparison shows that the simulated farfield pattern is in good agreement with the experimental results shown in (a), and indeed agrees well after scaling the angular range according to the different photon energies.

In Fig. 6, experimental farfield diffraction patterns of waveguides with different channel sizes are compared. As the lateral size is decreased (in horizontal direction) fewer modes can propagate, leading to a less structured farfield. The farfield diffraction patterns were recorded at 13.8 keV photon energy 5.2 m behind the waveguide by a Pilatus 300 K detector (Dectris) (`GINIX-2` setting). The waveguide chip was fabricated according to procedure IV (see Table I) and provides therefore an enhanced etching depth of approximately 70 nm. With comparable channel depths the reduction of the channel width leads to a noticeable change in the appearance of the farfield pattern. The recorded farfields exhibit a characteristic intensity pattern depending on the number of guides modes and hence the channel size. For broader channels (see Figs. 6(a) and 6(b)), the spatial frequencies in the farfield pattern along the horizontal direction are much higher than in vertical direction, since the confinement in the vertical direction is stronger than in the horizontal direction.

This is in agreement with the calculation, which predicts a higher number of guided modes due to the larger channel width. With decreasing channel width, the frequency of the intensity modulation in horizontal direction approaches that of the vertical direction, i.e., the farfield becomes smoother and more isotropic (see Fig. 6(d)). With its intensity plateau in the center and an integrated waveguide flux of $I_{wg} = 2.1 \times 10^8$ ph/s, the waveguide shown in Fig. 6(d) is well suited for imaging applications. Further progress is directed towards equal width and depth and a smaller channel size, while providing a sufficiently high transmission by avoiding structural defects.

IV. OUTLOOK AND SUMMARY

We have successfully fabricated and tested advanced two-dimensionally confining (channel) waveguides for hard x-rays, using a processing scheme involving e-beam lithography, reactive ion etching and wafer bonding. The specific requirements are very demanding, in view of the high aspect ratios needed to filter out one or several guided modes, since the attenuation for the radiative modes in the silicon cladding requires a thickness of several millimeters. Hence the required aspect ratios of channel length and lateral structure size can easily exceed 10^5, as in the present case for a 13 mm channel with a vertical cross section of 24 nm. Only by using an interferometric stage in the e-beam lithography system, these specifications can be met. Apart from the high aspect ratios, the fact that the structures have to be buried in order to function as channel waveguides presents a second considerable challenge. As shown here, the wafer bonding process is suitable to cap the channels efficiently, but only after some optimization, in particular regarding the high temperature annealing step. In this work, we have attempted to minimize the considerable interfacial diffusion and reaction processes at high temperatures as these were considered to be detrimental to the channel shape. In the future, if these effects can be controlled more precisely, they could also be used to the benefit. In fact, a well defined set of propagating modes exists for any cross sectional form, and shapes differing from rectangular shapes may even be of advantage for some applications. More importantly, the annealing can lead to a desirable reduction in structure size. Unfortunately, this effect has so far not been uniform over the length of the channel, leading to transmission losses, probably by scattering from channel inhomogeneities. In this respect, one should briefly address the tolerance in fabrication. Channel waviness, defects and interface roughness are all deviations from the ideal (design) structure, which - however - affect the optical properties very differently. It is known that low frequency waviness and broadened interfacial profiles (i.e., as resulting from surface diffusion or surface reactions) do not impede the propagation of well defined modes.[36] Contrarily, stitching errors and point defects can easily induce losses due to scattering of modes into the cladding. When traversing the full length of the structure, the scattered radiation is well absorbed in the cladding, and this effect will primarily lead to low transmission. Radiation scattered at higher angles, however, can escape the cladding, leading to the circular fringes around the central farfield cone, see Fig. 6(d). Importantly, due to the shallow angles of the internally reflected beam representing the modes, which are smaller than the critical angle of reflection α_c for silicon, the tolerance for defects (roughness, shape imperfections along the propagation direction) increases.[36] This is the reason why waveguides can be fabricated for the hard x-ray range at all.

Here, we have presented an approach to waveguide nanofabrication based on e-beam lithography and wafer bonding. The waveguides fabricated by this method have been demonstrated to be suitable x-ray optical components for coherent imaging[18] and nanodiffraction applications.[47] Refinement of the process, in particular in terms of the annealing process and channel inspection is under way. Notably the approach allows for a large variation in waveguide types: both tapered waveguide profiles and beam splitters can be realized. In the future, adaptation of the bonding process may make germanium accessible, which is interesting in view of high photon energy applications. Bonding has also been reported for quartz,[48] which would offer the opportunity of channel inspection with visible or infrared light.

ACKNOWLEDGMENTS

The authors would like to thank M. Reiche for helpful discussions on wafer bonding and K. Giewekemeyer for his contributions especially regarding the `ID22Ni` beamtime. Financial support by Deutsche Forschungsgemeinschaft through SFB 755 Nanoscale Photonic Imaging and by the Helmholtz society through Vernetzungsfonds VH-VI-403 is gratefully acknowledged.

[1]B. Niemann, D. Rudolph, and G. Schmahl, Opt. Commun. **12**, 160 (1974).
[2]C. David, B. Nöhammer, T. Weitkamp, H. H. Solak, A. Diaz, and J. F. van der Veen, AIP Conf. Proc. **705**, 764 (2004).
[3]W. Chao, B. D. Harteneck, J. A. Liddle, E. H. Anderson, and D. T. Attwood, Nature **435**, 1210 (2005).
[4]C. G. Schroer, Phys. Rev. B **74**, 033405 (2006).
[5]J. Maser, G. B. Stephenson, S. Vogt, W. Yun, A. Macrander, H. C. Kang, C. Liu, and R. Conley, *Optical Science and Technology, the SPIE 49th Annual Meeting. International Society for Optics and Photonics*, pp. 185–194 (2004).
[6]F. Döring, A.-L. Robisch, C. Eberl, M. Osterhoff, A. Ruhlandt, T. Liese, F. Schlenkrich, S. Hoffmann, M. Bartels, T. Salditt, and H.-U. Krebs, Opt. Express **21**, 19311 (2013).
[7]A. Snigirev, V. Kohn, I. Snigireva, and B. Lengeler, Nature **384**, 49 (1996).
[8]C. G. Schroer and B. Lengeler, Phys. Rev. Lett. **94**, 054802 (2005).
[9]C. G. Schroer, O. Kurapova, J. Patommel, P. Boye, J. Feldkamp, B. Lengeler, M. Burghammer, C. Riekel, L. Vincze, A. V. D. Hart, and M. Kuchler, Appl. Phys. Lett. **87**, 124103 (2005).
[10]P. Kirkpatrick and A. Baez, J. Opt. Soc. Am. **38**, 766 (1948).
[11]O. Hignette, P. Cloetens, W.-K. Lee, W. Ludwig, and G. Rostaing, J. Phys. IV France **104**, 231 (2003).
[12]E. Spiller and A. Segmüller, Appl. Phys. Lett. **24**, 60 (1974).
[13]Y. Feng, S. Sinha, E. E. Fullerton, G. Grübel, D. Abernathy, D. Siddons, and J. Hastings, Appl. Phys. Lett. **67**, 3647 (1995).
[14]S. Lagomarsino, W. Jark, S. Di Fonzo, A. Cedola, B. Mueller, P. Engström, and C. Riekel, J. Appl. Phys. **79**, 4471 (1996).
[15]M. J. Zwanenburg, J. F. Peters, J. H. H. Bongaerts, S. A. de Vries, D. L. Abernathy, and J. F. van der Veen, Phys. Rev. Lett. **82**, 1696 (1999).
[16]M. J. Zwanenburg, J. H. H. Bongaerts, J. F. Peters, D. O. Riese, and J. F. van der Veen, Phys. Rev. Lett. **85**, 5154 (2000).

[17]D. Pelliccia, I. Bukreeva, M. Ilie, W. Jark, A. Cedola, F. Scarinci, and S. Lagomarsino, Spectrochim. Acta, Part B **62**, 615 (2007).
[18]K. Giewekemeyer, H. Neubauer, S. Kalbfleisch, S. P. Krüger, and T. Salditt, New J. Phys. **12**, 035008 (2010).
[19]A. Ruhlandt, T. Liese, V. Radisch, S. P. Krüger, M. Osterhoff, K. Giewekemeyer, H. U. Krebs, and T. Salditt, AIP Adv. **2**, 012175 (2012).
[20]S. Di Fonzo, W. Jark, S. Lagomarsino, C. Giannini, L. De Caro, A. Cedola, and M. Müller, Nature **403**, 638 (2000).
[21]M. Müller, M. Burghammer, D. Flot, C. Riekel, C. Morawe, B. Murphy, and A. Cedola, J. Appl. Crystallogr. **33**, 1231 (2000).
[22]F. Pfeiffer, C. David, M. Burghammer, C. Riekel, and T. Salditt, Science **297**, 230 (2002).
[23]A. Jarre, C. Fuhse, C. Ollinger, J. Seeger, R. Tucoulou, and T. Salditt, Phys. Rev. Lett. **94**, 074801 (2005).
[24]C. Fuhse, C. Ollinger, and T. Salditt, Phys. Rev. Lett. **97**, 254801 (2006).
[25]C. Bergemann, H. Keymeulen, and J. F. van der Veen, Phys. Rev. Lett. **91**, 204801 (2003).
[26]H. Mimura, S. Handa, T. Kimura, H. Yumoto, D. Yamakawa, H. Yokoyama, S. Matsuyama, K. Inagaki, K. Yamamura, Y. Sano, K. Tamasaku, Y. Nishino, M. Yabashi, T. Ishikawa, and K. Yamauchi, Nat. Phys. **6**, 122 (2010).
[27]S. Di Fonzo, W. Jark, G. Soullie, A. Cedola, S. Lagomarsino, P. Cloetens, and C. Riekel, J. Synchrotron Radiat. **5**, 376 (1998).
[28]S. Eisebitt, J. Lüning, W. F. Schlotter, M. Lörgen, O. Hellwig, W. Eberhardt, and J. Stöhr, Nature **432**, 885 (2004).
[29]G. J. Williams, H. M. Quiney, B. B. Dhal, C. Q. Tran, K. A. Nugent, A. G. Peele, D. Paterson, and M. D. de Jonge, Phys. Rev. Lett. **97**, 025506 (2006).
[30]L. De Caro, C. Giannini, S. Di Fonzo, W. Jark, A. Cedola, and S. Lagomarsino, Opt. Commun. **217**, 31 (2003).
[31]W. Jark and S. Di Fonzo, J. Synchrotron Radiat. **11**, 386 (2004).
[32]I. Bukreeva, A. Popov, D. Pelliccia, A. Cedola, S. B. Dabagov, and S. Lagomarsino, Phys. Rev. Lett. **97**, 184801 (2006).
[33]C. Fuhse and T. Salditt, Appl. Opt. **45**, 4603 (2006).
[34]C. Fuhse and T. Salditt, Opt. Commun. **265**, 140 (2006).
[35]S. Panknin, A. K. Hartmann, and T. Salditt, Opt. Commun. **281**, 2779 (2008).
[36]M. Osterhoff and T. Salditt, Opt. Commun. **282**, 3250 (2009).
[37]S. P. Krüger, K. Giewekemeyer, S. Kalbfleisch, M. Bartels, H. Neubauer, and T. Salditt, Opt. Express **18**, 13492 (2010).
[38]M. Poulsen, F. Jensen, O. Bunk, R. Feidenhans'l, and D. W. Breiby, Appl. Phys. Lett. **87**, 261904 (2005).
[39]A. Kohlstedt, S. Kalbfleisch, T. Salditt, M. Reiche, U. Gösele, E. Lima, and P. Willmott, Appl. Phys. A **91**, 7 (2008).
[40]U. Gösele and Q.-Y. Tong, Annu. Rev. Mater. Sci. **28**, 215 (1998).
[41]B. Cord, J. Lutkenhaus, and K. K. Berggren, J. Vac. Sci. Technol. B **25**, 2013 (2007).
[42]X. X. Zhang and J.-P. Raskin, J. Microelectromech. Syst. **14**, 368 (2005).
[43]W. Kern and D. Puotinen, RCA Rev. **31**, 187 (1970).
[44]W. P. Maszara, G. Goetz, A. Caviglia, and J. B. McKitterick, J. Appl. Phys. **64**, 4943 (1988).
[45]S. Kalbfleisch, M. Osterhoff, K. Giewekemeyer, H. Neubauer, S. P. Krüger, B. Hartmann, M. Bartels, M. Sprung, O. Leupold, F. Siewert, and T. Salditt, AIP. Conf. Proc. **1234**, 433 (2010).
[46]S. Kalbfleisch, H. Neubauer, S. P. Krüger, M. Bartels, M. Osterhoff, D. D. Mai, K. Giewekemeyer, B. Hartmann, M. Sprung, and T. Salditt, AIP Conf. Proc. **1365**, 96 (2011).
[47]C. Krywka, H. Neubauer, M. Priebe, T. Salditt, J. Keckes, A. Buffet, S. V. Roth, R. Döhrmann, and M. Müller, J. Appl. Crystallogr. **45**, 85 (2012).
[48]A. Grosse, M. Grewe, and H. Fouckhardt, J. Micromech. Microeng. **11**, 257 (2001).